Implications of hydrothermal flow-through experiments on deep geothermal energy utilization

Xiang-Zhao Kong, Allan M.M. Leal, Martin O. Saar

Institute of Geophysics, ETH-Zurich, Sonneggstrasse 5, 8092 Zurich, Switzerland

xkong@ethz.ch

Keywords: Geothermal, Reactive transport, Fluid-rock reaction, Reactive surface area, Dissolution.

ABSTRACT

Utilization of underground reservoirs for geothermal energy extraction, particularly using CO_2 as a working fluid, requires an in-depth understanding of fluid, solute (e.g., dissolved CO_2 and minerals), and energy (heat, pressure) transport through geologic formations. Such operations necessarily perturb the chemical, thermal, and/or pressure equilibrium between native fluids and rock minerals, potentially causing mineral dissolution and/or precipitation reactions with often immense consequences for fluid, solute, and energy transport, injectivity, and/or withdrawal in/from such reservoirs. The involved physico-chemico-thermo-mechanical processes often lead to modifications of permeability, one of the most variable and important parameters in terms of reservoir fluid flow and related advective solute/reactant and heat transport. Importantly, the amount of mineral dissolution/precipitation that can cause orders of magnitude in permeability reduction can be very small, if minerals are removed or deposited in pore throats or narrow fracture apertures. This potentially has detrimental consequences for geothermal energy usage.

However, analysing, understanding, and predicting reservoir evolution and flow properties are non-trivial, as they depend on complex chemical, thermodynamic, and fluid-dynamic feedback mechanisms. To achieve these goals, it requires the integration and extrapolation of thermodynamic, kinetic, and hydrologic data from many disparate sources. The validity, consistency, and accuracy of these data-model combinations are unfortunately often incomparable due to the relative scarcity of appropriate parameterizations in the literature. Here, we present some results of hydrothermal flow-through experiments on rock core samples. During the experiments, we fixed the flow rates, confinement and outlet pore-fluid pressures, and recorded inlet pore-fluid pressure. We also analysed the outlet fluid chemistry samples throughout the experiments and imaged our rock cores before and after the flow-through experiments using X-Ray Computed Tomography (XRCT). With all these data, we are able to interpret the changes in permeability, porosity, and (reactive) surface area at the core scale.

1. INTRODUCTION

Geothermal energy is thermal energy generated mainly from radioactive decay and heat loss from Earth's formation (The KamLAND collaboration, 2011). The Earth has an estimated internal heat content of 10^{31} joules, with a heat flow to the Earth surface by conduction at a rate of 44.2 terawatts (TW) (Pollack et al., 1993; Fridleifsson et al., 2008; Bayer et al., 2013). A mean geothermal gradient of at least 35°C/km, maintained to a depth of 3-4 km, is estimated to be the economic minimum requirement for geothermal energy "mining" (Rollin & Institute of Geological Sciences, 1982). Ninety-nine percent of the earth's volume has temperatures higher than 1000 °C, with only 0.1% at temperatures lower than 100 °C (Bayer et al., 2013). Therefore, geothermal energy is sufficiently large and immense, and counted among renewable energies with great potential for the future (Blackwell et al., 2006; Tester et al., 2006; Rybach, 2010; Bahadori et al., 2013).

Harvesting the energy from deep geothermal resources involves circulating fluids, which will be heated while transmitted through the hot subsurface reservoirs, and extracting their heat at the surface power plants for electricity generation or through heat exchangers for direct use (Bertani, 2012; Chamorro et al., 2012; DiPippo, 2012; Hirschberg et al., 2014). Within recent years, many (European and other) sites have been investigated and some developed to determine if they are suitable for economic geothermal energy development (see e.g., Kohl et al., 2003; Bayer et al., 2013; Schill et al., 2015). The sustainable operation of the geothermal system lies on the transmissivity and the fluid's heat content/temperature of the reservoirs. One of the major limitations for geothermal energy development is low natural fluid productivity, particularly in low- and medium-enthalpy reservoirs. In order to increase the magnitude of fluid and heat productivity to levels that enable economic use of natural geothermal systems, permeability stimulation treatments are widely used. Permeability may be increased by hydraulic, thermal, and/or acid

stimulation techniques. However, new well designs, adapted from the oil and gas industry, have also been developed to enhance the performance of such enhanced or engineered geothermal systems (EGS). Chemical stimulation is one of the engineering treatment to improve the transmissivity and productivity of the subsurface reservoirs (Portier et al., 2007; Rose et al., 2007; Nami et al., 2008; Portier et al., 2009; Taron & Elsworth, 2009; Schill et al., 2015). In particular, Xu (2010) numerically investigated the feasibility of using carbon dioxide (CO_2) as a stimulation agent for EGS, because dissolution of CO_2 into formation fluids reduces their pH, resulting in the dissolution of minerals (Luquot et al., 2012; Luhmann et al., 2014; Tutolo et al., 2014; Tutolo et al., 2015; Kong & Saar, in prep.). In addition, CO_2 may simultaneously be used as a working fluid (Figure 1) to extract geothermal energy (Brown, 2000; Pruess, 2006), as a form of carbon capture, utilization, and storage (CCUS) to mitigate global climate change that is caused by increasing atmospheric CO_2 concentration (IPCC, 2005).

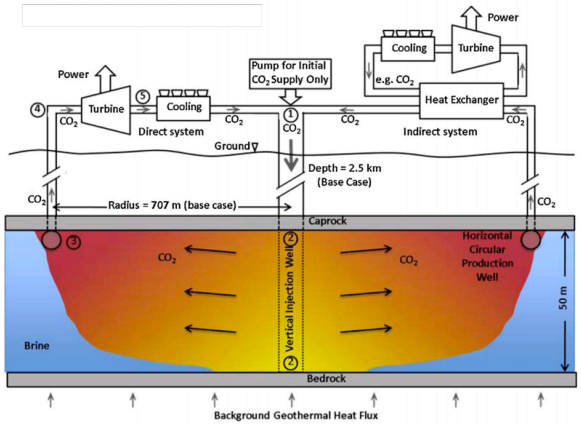

Figure 1: Illustration showing a vertical cross section through one possible implementation of a simplified radial-reservoir CO_2-Plume Geothermal (CPG) system (after Randolph & Saar, 2011; Saar et al., 2012-2015; Garapati et al., 2014; Garapati et al., 2015), implemented in a deep saline aquifer.

Nonetheless, such operations of subsurface reservoirs necessarily perturb the chemical, thermal, and/or pressure equilibrium between native fluids and rock minerals, potentially causing mineral dissolution and/or precipitation reactions with often immense consequences for fluid, solute, and energy transport, injectivity, and/or withdrawal in/from such reservoirs. To delineate these coupling processes, hydrothermal flow-through experiment on rock cores is one of the state-of-the-art approaches allowing us not only to examine relevant chemical reactions due to mineral dissolution and precipitation, but also to provide critical insight on permeability evolution and associated fluid flow. Understanding these complex geochemical processes involved in the evolution of reservoir properties requires determination of mineral reactivity, including kinetic reaction rate and reactive surface area of minerals. Typically, kinetic reaction rates are measured in the laboratory in well-mixed reaction systems using crushed mineral grains (see e.g., Golubev et al., 2005; Pokrovsky et al., 2005) and their reactive surface area, usually measured by the Brunauer-Emmet-Teller (B.E.T) method (Brunauer et al., 1938) or simply based on geometric area (Gautier et al., 2001). However, mineral surface areas of natural rocks are generally poorly characterized (Helgeson et al., 1984; White & Peterson, 1990; Nagy et al., 1999; Washton et al., 2008; Peters, 2009; Landrot et al., 2012; Luhmann et al., 2014) and incomparable to the ones measured in laboratory experiments (White & Peterson, 1990; Hajash et al., 1998; Li et al., 2014; Luhmann et al., 2014). Moreover, lab-measured kinetic reaction rates and reactive surface areas are, unfortunately, related to each other because the lab-measured kinetic reaction rate is typically normalized to reactant mineral surface area. Although many studies focus on mineral-specific dissolution rates, very few laboratory studies have explored the complexities of whole rock reaction kinetics (White et al., 1999; White & Brantley, 2003; Gong et al., 2012; Li et al., 2014; Luhmann et al., 2014; Tutolo et al., 2014). For example, Luquot and Gouze (2009) conducted a series of flow-through experiments by flooding brines, with dissolved CO_2, through limestone cores. With fluid chemistry from the fluid samples and pre-defined porosity-surface area relationships, they can determine changes in surface area and porosity-permeability relationships through fits of calculated porosity over time, employing mass balance calculations. Gouze and Luquot (2011) used 3D X-ray micro-tomography images to validate the porosity-surface area power-law model of Gouze and Luquot (2011) and to determine the relative contribution of flow path tortuosity and hydraulic radius to porosity-permeability relationships. Similarly, Luhmann et al. (2014) conducted hydrothermal flow-through experiments of single-pass injection of CO_2-charged brine on nine dolomite rock cores to examine fluid-rock reactions under geologic carbon sequestration conditions. Following the fitting procedure of Luquot and Gouze (2009), they employed a power-law relationship between reactive surface area and porosity to determine changes in these two quantities.

In (Luquot & Gouze, 2009; Gouze & Luquot, 2011; Luquot et al., 2012; Luhmann et al., 2014; Tutolo et al., 2014; Tutolo et al., 2015), fits of calculated porosity over time are the cornerstones of the subsequent analysis. However, porosities of core samples in their works were determined by X-ray Compted Tomography (XRCT) data sets and mass balance calculations. Thus the calculated porosities will be affected by the XRCT resolution and the thresholding applied on the XRCT data. Moreover, rock samples were imaged ex-situ, i.e., not at elevated temperatures and pressures. This will introduce further off-set on the porosity calculation using XRCT data. Although Luhmann et al. (2014) have performed Monte-Carlo analysis on uncertainty estimation of the

fitting parameters, new measurements (using water saturation) of porosity for the dolomite rock cores show a much higher value compared to the porosity determined using XRCT data, according to private communications with Dr. Luhmann and Dr. Tutolo. Therefore, it is necessary to re-visit the experimental results and investigate the effect of initial porosity on the fitting parameters. Moreover, we extend our discussions on implications of our findings to EGS.

2. METHODOLOGY

The flow-through system used in (Luhmann et al., 2014), also previously described in (Luhmann et al., 2012; Tutolo et al., 2014), employs Teledyne ISCO syringe pumps to provide fluid flow through cylindrical core smaples at pre-defined flow rates, back pore-fluid pressure (set to 150 bar), as well as confinement pressure (set to 200 bar) around the dolomite sample (see Figure 2). A total number of 9 experiments were conduted at five levels of flow rates, namely, 0.01, 0.0316, 0.1, 0.316, and 1 ml/min, to assess relationships of porosity-surface area and porosity-permeability over two orders of magnitude of flow rates (see Table 1). Temperature during all 9 experiemtns were maintained to 100 °C by four eletronic Watlow band heaters. Core samples were first wrapped by 0.8 mm-thick Teflon FEP sheath, and then by 0.05 mm-thick stainless stell foil around the Teflon sheath to minimize CO_2 diffusion into the confinning fluid.

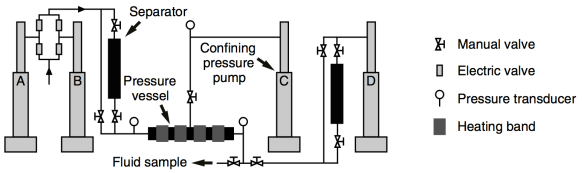

Figure 2: Flow-through system used in (Luhmann et al., 2014). The double-pump (A and B) pushed the CO_2-charged brine sitting in a separator through the core sample, housed in a pressure vessel. Pump C provided constant confinement pressure around the sample, and Pump D for the constant outlet pressure. Inlet and outlet pressures were monitored by pressure transducers.

Experiments used dolomite cores cut from the Madison Limestone, collected from an outcrop in Layton Canyon in the Black Hills of South Dakota. The molecular formula of these dolomite cores was estimated from oxide analysis using an inductively coupled plasma-optical emission spectrometer (ICP-OES), namely, $Ca_xMg_y(CO_3)_2$, where x=1.02 and y=0.98 were suggested. The cores were dried in an oven at 60 °C both pre- and post-experiment before they were weighed to determine mass change from fluid-rock reaction.

The experimental fluid in the upstream separator consisted of a 0.92 ml NaCl/kg solution (1 molal NaCl) with a 0.6 mol CO_2/kg solution (i.e., 0.65 molal CO_2 or 129 pCO_2), equivalent to ~80% saturation concentration, calculated according to CO_2 solubility model of (Duan & Sun, 2003; Duan et al., 2006). During each experiment, fluid samples were collected at the the outlet of pressure vessel to constrain fluid-rock interaction. Major dissolved cations of all collected fluid samples were analysed using ICP-OES, and major dissolved anions of collected fluid samples were only analysed for Experiments 1 and 6 using ion chromatography.

A series of pressure gradients and flow rates was used during deionized (DI) water flow both before and after each experiment to confirm the presence of laminar flow and to provide better resolution for measurement of initial and final bulk permeability.

Table 1: Nine flow-through experiments labeled from No. 1 to 9 on dolomite samples with a mean diameter of 12.78±0.044 mm and a mean length of 25.94±0.413 mm. Q_v: the volumetric flow rate, t_d: duration, Δm: loss of mass due to dissolution, k_0: initial permeability, k_f: final permeability. (modified from (Luhmann et al., 2014))

No.	Q_v (ml/min)	t_d (min)	Δm (g)	k_0 (m^2)	k_f (m^2)
1	1.0	61	0.146	$3.7x10^{-16}$	$2.79x10^{-15}$
2	0.316	180	0.114	$1.31x10^{-15}$	$2.12x10^{-14}$
3	0.1	408	0.112	$5.7x10^{-16}$	$4.3x10^{-15}$
4	0.1	350	0.094	$7.7x10^{-16}$	$7.9x10^{-15}$
5	0.1	427	0.118	$7.5x10^{-16}$	$1.07x10^{-14}$
6	0.1	367	~0.1	$4.5x10^{-16}$	$2.05x10^{-15}$
7	0.0316	2222	0.162	$1.47x10^{-16}$	$3.8x10^{-15}$
8	0.01	12962	0.273	$4.5x10^{-16}$	$1.32x10^{-15}$
9	0.01	12742	0.268	$2.89x10^{-16}$	$1.32x10^{-15}$

3. RESULTS AND DISCUSSION

Real-time bulk permeability, k, can be determined using Darcy's law:

$$k = -Q_v\mu_f/(A\nabla P)\,, \qquad [1]$$

where A is the core cross-sectional area, ∇P is the pressure gradient across the core length, and μ_f is the fluid dynamic viscosity which was taken conservatively to be 323.1 μPa s for a 1 molal NaCl solution at 100 °C and 150 bar (Kestin et al., 1981; Mao & Duan, 2009). Permeability enhancement was observed for all nine experiments, with increase ranging from ~2.6 times to more than an order of magnitude (see Table 1 and Inset in Figure 3). We argue that this enhancement in permeability was induced by mineral dissolution, as indicted by loss of

mass shown in Table 1. Note that noise in permeability profiles could be caused by laboratory temperature fluctuations, collection of fluid samples, and small pressure drop across the inlet and the outlet, particularly for experiments at low flow rates. Figure 3 shows the the incubation time versus the volumetric flow rates. The incubation time is defined as the duration from time zero to the time when permeability starts to increase. We notice that the incubation time decreases sharply as volumetric flow rate increases from 0.0316 to 0.1 ml/min, then steadily levels off when volumetric flow rate increase further. The incubation time seems to directly link to the dissolution patterns occurred during the experiments. As shown in Fig. 4 in (Luhmann et al., 2014), three-dimensional (3D) XRCT images illustrate that dissolution pattern changes from conical dissolution at the lowest flow rate to dominant dissolution at median flow rate, and then to ramified/uniform dissolution at highest flow rate (see e.g., Hoefner & Fogler, 1988; Fredd & Fogler, 1998; Fredd & Fogler, 1999). For the ramified/uniform dissolution, mineral-fluid reactions tend to occur homogeneously and largely use the pre-existing pore networks. Therefore, this type of dissolution produces less incubation time. In contrast, the conical dissolution mainly results from mineral-fluid reactions at the upstream end. This would take much longer time to its effects on permeability because the bulk permeability was still controlled by the intact portion of core at the downstream end.

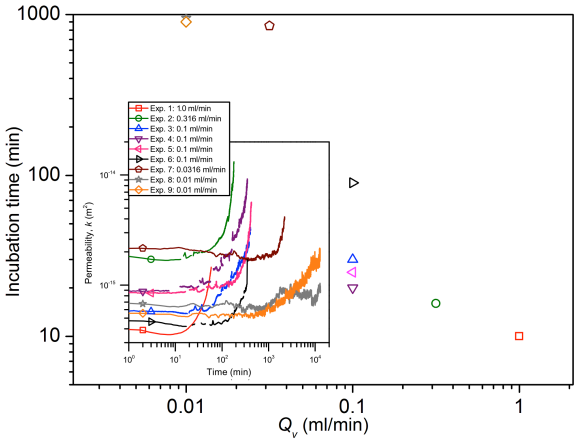

Figure 3: Incubation time versus volumetric flow rates. Inset: changes of permeability as a function of time (after Luhmann et al., 2014).

Moreover, permeability heterogeneities in rock samples will cause various transport patterns of mass transfer (e.g., Kong & Saar, 2013). This effect is also shown in the variations of incubation time at a volumetric flow rate of 0.1 ml/min in Figure 3. As shown in Fig. 8 in (Luhmann et al., 2014), different dominant dissolution patterns were observed in 4 experiments at a volumetric flow rate of 0.1 ml/min.

One of the possible ways to reduce the off-set comparison due to initial permeability heterogeneities is to compare the permeability enhancement using the normalized permeability, k/k_0, as shown in Figure 4.

The rate of the normalized permeability increment, $\mathrm{d}(k/k_0)/\mathrm{d}V_{in}$, first increases with the increase in volumetric flow rate to a maximum (at 0.1 ml/min), then decreases as the volumetric flow rate increases further, where V_{in} is the injection fluid volume. It is clearly shown that a flow rate of 0.1 ml/min produced the most effective permeability enhancement compared to the other flow rates in all the conducted experiments. In particular, the normalized permeability, k/k_0, increases the fastest in Exp. 4.

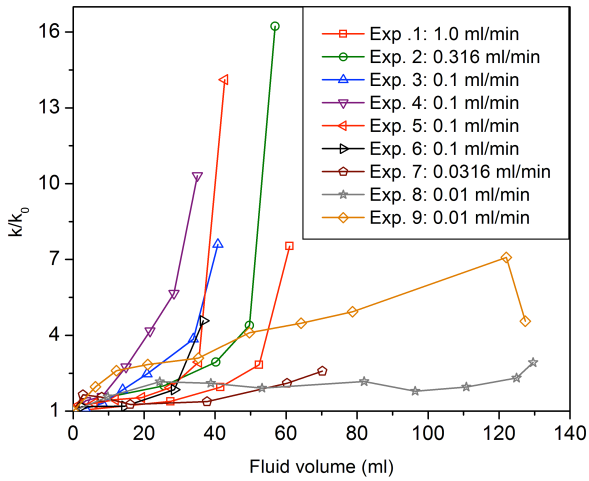

Figure 4: Evolutions of normalized permeability, k/k_0, as a function of injection fluid volume (= volumetric flow rate × time).

As stated above, changes of permeability in the samples are attributed to pore structure changes, *i.e.*, porosity changes. The changes of porosity, $\overline{\Delta\phi}$, can be determined by:

$$\overline{\Delta\phi} = \bar{\phi}(t) - \bar{\phi}^* = \frac{V_{dolomite}(t)}{V_{core}}, \qquad [2]$$

where $\bar{\phi}(t)$ is the sample-averaged porosity at time t, $\bar{\phi}^*$ is the initial sample-averaged porosity, $V_{dolomite}(t)$ is the volume of dissolving dolomite at time t, V_{core} is the total core volume, *i.e.*, product of the cross-sectional area and the length of core sample. Based on mass balance and measured Ca and Mg concentrations, $V_{dolomite}(t)$ is given by:

$$V_{dolomite}(t) = 0.5\upsilon Q_v \rho_f \int_{\tau=0}^{\tau=t} \left[x\Delta C_{\mathrm{Ca}}(\tau) + y\Delta C_{\mathrm{Mg}}(\tau) \right] \mathrm{d}\tau, \qquad [3]$$

where $\upsilon = 6.36\times10^{-5}$ m^3/mol is the dolomite molar volume, ρ_f is the fluid density, ΔC_{Ca} and ΔC_{Mg} are the outlet Ca and Mg concnetrations, respectively. Given the Ca and Mg concentrations in Table 3 in (Luhmann et al., 2014), $V_{dolomite}(t)$ can be easily calculated.

Figure 5 reports the changes of porosity as a function of injection fluid volume, based on equation [2]. The increase rate of changes of porosity could be grouped into two categories sorted by volumetric flow rates, namely, a rapid growth group with flow rates smaller than 0.316 ml/min, and a slow growth group with flow

rate larger than 0.1 ml/min. In each group, the same amount of injection fluid will result in the similar changes in porosity, regardless of flow rates. For the rapid growth group, a clear transition from non-linear to linear growth occurs at fluid injection volume of about 20 ml.

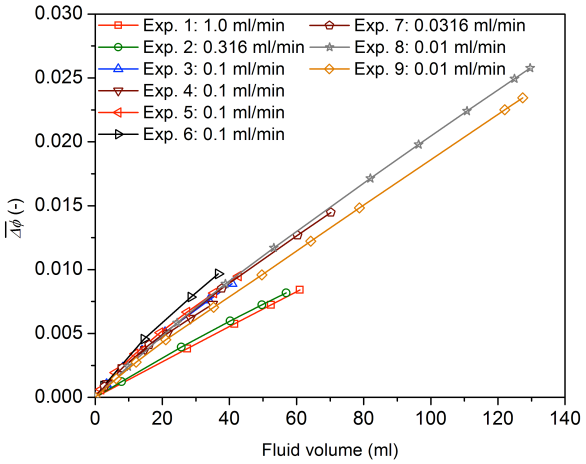

Figure 5: Changes of porosity as a function of injection fluid volume.

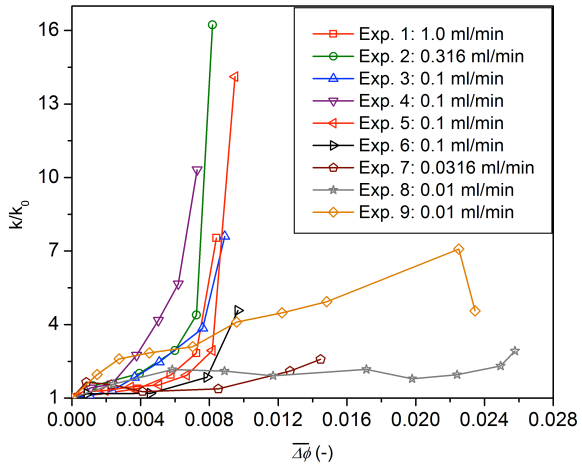

Figure 6: Evolutions of normalized permeability, k/k_0, as a function of porosity change.

Figure 6 represents the time-resolved normalized permeability versus the porosity change. Experiment with flow rates greater than 0.0316 ml/min displays a relatively larger enhancement of permeability ratio per increase of porosity. Figure 6 clearly illustrates permeability complexity induced by a combination of several parameters, including the geometry of pores and throats, as well as their connectivity. If the dissolution occurs at critical throats, very little changes of porosity can result in dramatic changes in permeability, as shown the growing enhancement of normalized permeability observed in experiments with flow rates larger than 0.0316 ml/min.

Although we can use the B.E.T method to determine the physical total surface area of void space, because of the complexity of fluid flow through void space, some portions of the total surface area receive large percentages of fluid, where reactions are likely controlled by mass transfer rate at the fluid-mineral interface; while fluids in other portions of the surface area are stagnant, where reactions are likely tranport-limited. This hydrology complexity will be partially resposible for the observed off-set between surface area measured by the B.E.T. method and surface area suggested by fluid chemistry (White & Peterson, 1990; Hajash et al., 1998; Li et al., 2014; Luhmann et al., 2014). To determine pore volume-normalized reactive surface area, $\overline{\sigma}(t)$ at time t, a power-law relationship between reactive surface area and porosity was employed (Luquot & Gouze, 2009; Gouze & Luquot, 2011; Luquot et al., 2012; Luhmann et al., 2014):

$$\frac{\overline{\sigma}(t)}{\overline{\sigma}^*} = \left(\frac{\overline{\phi}(t)}{\overline{\phi}^*}\right)^{-w}, \qquad [4]$$

where w is a geometrical exponent and $\overline{\sigma}^*$ is the initial pore volume-normalized reactive surface area. By linking the sample-averaged porosity to the sample-averaged mass trasnfer rate using transition state theory (Luquot & Gouze, 2009; Gouze & Luquot, 2011; Luquot et al., 2012; Luhmann et al., 2014), the values of w and $\overline{\sigma}^*$ can be determined through curve-fitting of time-resolved porosity calculated in equation [2] and the mass balance calculation in equation [3].

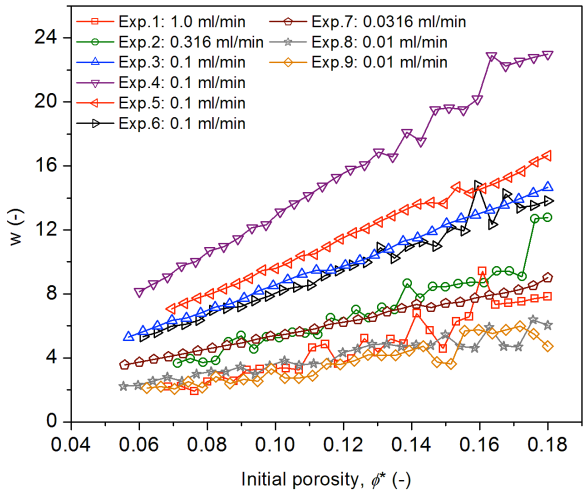

Figure 7: Fitting parameter, w, as a function of the initial porosity.

We have noticed that there were no analysis on the dependency of w on initial porosity in Luquot & Gouze (2009); Gouze & Luquot (2011); Luquot et al. (2012); and Luhmann et al. (2014). The major uncertainty of porosity determination likely originated from XRCT data, including XRCT resolution, thresholding, and ex-situ imaging. By assuming that initial porosity of the nine dolimite rock samples varies from the XRCT-determined porosity to a porosity of 18% (the highest value determined using water-saturation method, through private communication with Dr. Luhmann and Dr. Tutolo), Figure 7 reports the dependency of w on the initial porosity. The value of w steadily increases with an

increasement of initial porosity. Experiments with higher value of *w* appear to have higher increase rates of *w* per increase of initial porosity. In particular, the highest values of *w* and $^{dw/d\bar{\phi}^*}$ both appear in Exp. 4 with a flow rate of 0.1 ml/min, where the greatest enhancement of normalized permeability per increase of porosity was observed (see Figure 6). As interpreted in Luquot & Gouze (2009), *w* characterises the time-resolved efficiency of the dissolution, namely permeabilitiy increase rate per increase of porosity. Higher *w* indicates greater efficiency of the dissolution. Figure 7 depicts that the highest efficiency of dissolution is observed in Luhmann et al. (2014) with experiments of flow rate of 0.1 ml/min, which is consist with results of tortuosity calculation in Luhmann et al. (2014). Therefore, Figure 7 suggests that a higher initial porosity requires a higher dissolution effciency at the same flow rate.

In contrast, $\bar{\sigma}^*$ decreases with the increase of initial porosity, as shown in Figure 8. Although all the curves appear to be parallel to each other in Figure 8, the decrease rate of $\bar{\sigma}^*$ per increase of initial porosity, $^{d\bar{\sigma}^*/d\bar{\phi}^*}$, actually decreases with the increase of $\bar{\sigma}^*$, because Figure 8 is a semi-log plot. It is worth to note that $\bar{\sigma}^*$ is not solely a geometry-controlled parameter, but also controlled by the chemical disequiilibrium of inlet fluid, as well as fluid flow complexity (Luquot & Gouze, 2009; Luhmann et al., 2014). In that sense, Figure 8 also describes the effect of geometry, indicated by sample-averaged porosity, on $\bar{\sigma}^*$. The diffecence between the XRCT-determined porosity and the porosity determined by water-saturation method is apparently not visible to the current XRCT resolution. This difference is likely contributed by the micropores in the solid around the macropores that are visable to the current XRCT resolution. Therefore, we expect an increase of the physical surface area. However, Figure 8 shows that the increase of the initial porosity in the fitting of the calculated porosity is not followed by an increase of $\bar{\sigma}^*$. Thus, Figure 8 could further imply that although the initial porosity increases, the hydraulic accessable reactive surface area decreases.

Figure 9 shows that, as $\bar{\phi}^*$ increases, the two independent fitting parameters shift from the left to the right of the figure. It suggests that to produce the same dissolution rate, represented by the rate of porosity increment, $\bar{\sigma}^*$ needs to be reduced and simultaneously *w* needs to be increased, as the initial porosity increases. This implies that the effect of the decrease of $\bar{\sigma}^*$ on the dissolution rate is mitigated by the increase of dissolution effeciency. Moreover, as the initial porosity increases from 0.056 to 0.18, three groups of dissolutioin regimes (characterized by the relationship between $\bar{\sigma}^*$ and *w*) are clearly identified: (1) upper group with flow rates between 0.1 to 1.0 ml/min, (2) middle group with flow rate of 0.0316 ml/min, and (3) lower group with flow rate of 0.01 ml/min, as shown in Figure 9.

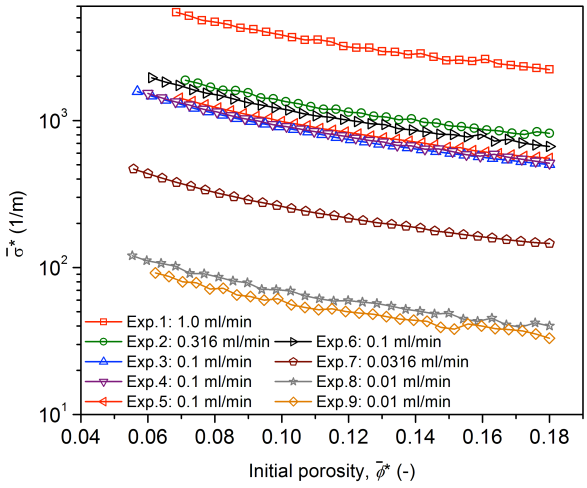

Figure 8:The fitted initial reactive surface area, $\bar{\sigma}^*$, as a function of the initial porosity.

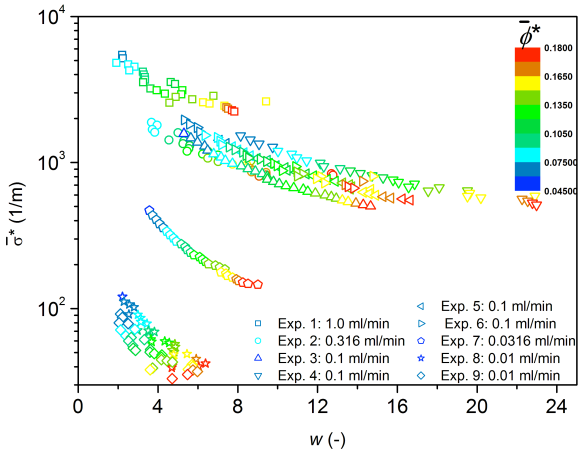

Figure 9: Dependency of the relationship between the fitted initial reactive surface area, $\bar{\sigma}^*$, and the fitted parameter, *w*, on initial porosity.

As we stated in Section 1, one of the major limitations for geothermal energy development is low natural fluid productivity, particularly in low- and medium-enthalpy reservoirs. The reported acidic stimulation treatments on permeability in this work are highly relevant to EGS. Harvesting the energy from deep geothermal resources involves circulating fluids which will be heated while transmitted through the hot subsurface reservoir. If the permeabilities of the geothermal reservoirs are sufficiently high, the advective heat transfer is dominant in EGS; otherwise, the conductive heat transfer is dominant. The time-resolved temperature, *T*, in a porous medium can be described as (Saar, 2011)

$$\frac{\partial\left[\bar{\phi}\rho_f c_f+\left(1-\bar{\phi}\right)\rho_s c_s\right]T}{\partial t}=\nabla\cdot\left[\frac{\rho_f c_f T}{\mu_f}\mathbf{k}\cdot\nabla\left(P+\rho_f g z\right)\right]+\nabla\cdot\left(\mathbf{K}_{T_m}\cdot\nabla T\right)+S_h \quad [5]$$

where *P* is pore-fluid pressure, *g* is gravitational acceleration, z is elevation above some reference level, S_h is heat source/sink, *c* is specific heat capacity,

$\mathbf{K}_T$ is thermal conductivity, and subscripts *f*, *s*, and *m* denote fluid, sloid, and fluid-solid mixed properties. On the right-hand side of equation [5], the first term represents advective heat transfer induced by fluid flow, and the second term describes the conductive heat transfer. For consolidated rock samples, previous measurements show that thermal conductivity decreases as porosity increases (Woodside & Messmer, 1961a, 1961b). It suggests that the advective heat transfer will be continuously enhanced because of the increment of permeability and the conductive heat transfer will be further limited due to the decrease of the mixed thermal conductivity with dissolution reaction progress. Similar to the effect of dissolution pattern on the enhancement of permeability, different dissolution patterns will have distinct effects on the mixed thermal conductivity. Since we are interested in harvesting the energy from deep geothermal resources, ideally we would like to enhance both the conductive and advective heat transfer, or at least minimize the reduction of conductive heat transfer if not possible to maintain it. Therefore, further work should include investigations of relationship between the mixed thermal conductivity and porosity and surface area. This will help to determine which dissolution pattern will be the preferred one, *i.e.*, with the highest $dk/d\Delta\phi$ and the lowest $dk_T/d\Delta\phi$. This eventually facilitates the development of best practices and tools for the assessment of effectiveness of chemical/acid treatments for different reservoir conditions.

4. CONCLUSIONS

We have re-visited the experimental results of injection of CO_2-charged brine into nine dolomite cores at a temperature of 100 °C and back pore-fluid pressure of 150 bar with fluid flow rates that spanned two orders of magnitude (from 0.01 ml/min to 1.0 ml/min). We found that the incubation time decreases sharply as volumetric flow rate increases from 0.0316 to 0.1 ml/min, then steadily levels off when volumetric flow rate increase further. Experiment at flow rates greater than 0.0316 ml/min displays a growing enhancement of permeability ratio per increase of porosity. While experiments at the lowest flow rates were characterized by a lower permeability enhancement rate.

We refit the calculated porosity data with a guessing initial porosity that varies from XRCT-determined porosity to a porosity determined by water saturation method. We found that the value of *w* steadily increases with an increase of initial porosity. Experiments with higher value of *w* appear to have higher increase rates of *w* per increase of initial porosity. In contrast, the fitted initial reactive surface area decreases with the increase of the guessing initial porosity. This implies that the effect of the decrease of the fitted initial reactive surface area on the dissolution rate is mitigated by the increase of dissolution effeciency.

Our experimental results suggest that the advective heat transfer will be continuously enhanced because of the increment of permeability and the conductive heat transfer will be further limited due to the decrease of the mixed thermal conductivity with dissolution reaction progress. However, further investigations are needed to determine the dependency of the mixed thermal conductivity on porosity increment and surface area.

REFERENCES

Bahadori, A., Zendehboudi, S., & Zahedi, G. RETRACTED: A review of geothermal energy resources in Australia: Current status and prospects. Renewable and Sustainable Energy Reviews, 21, (2013), 29-34.

Bayer, P., Rybach, L., Blum, P., & Brauchler, R. Review on life cycle environmental effects of geothermal power generation. Renewable and Sustainable Energy Reviews, 26, (2013), 446-463.

Bertani, R. Geothermal power generation in the world 2005–2010 update report. Geothermics, 41, (2012), 1-29.

Blackwell, D. D., Negraru, P. T., & Richards, M. C. Assessment of the enhanced geothermal system resource base of the United States. Natural Resources Research, 15(4), (2006), 283-308.

Brown, D. W. A hot dry rock geothermal energy concept utilizing supercritical CO_2 instead of water, (2000), Paper presented at the Proceedings.

Brunauer, S., Emmett, P. H., & Teller, E. Adsorption of gases in multimolecular layers. Journal of the American Chemical Society, 60(2), (1938), 309-319.

Chamorro, C. R., Mondéjar, M. E., Ramos, R., Segovia, J. J., Martín, M. C., & Villamañán, M. A. World geothermal power production status: Energy, environmental and economic study of high enthalpy technologies. Energy, 42(1), (2012), 10-18.

DiPippo, R. Geothermal power plants: principles, applications, case studies and environmental impact: Butterworth-Heinemann, (2012).

Duan, Z., & Sun, R. An improved model calculating CO_2 solubility in pure water and aqueous NaCl solutions from 273 to 533 K and from 0 to 2000 bar. Chemical Geology, 193(3), (2003), 257-271.

Duan, Z., Sun, R., Zhu, C., & Chou, I.-M. An improved model for the calculation of CO_2 solubility in aqueous solutions containing Na^+, K^+, Ca^{2+}, Mg^{2+}, Cl^-, and SO_4^{2-}. Marine Chemistry, 98(2), (2006), 131-139.

Fredd, C., & Fogler, H. Optimum conditions for wormhole formation in carbonate porous media: Influence of transport and reaction. SPE Journal, 4(03), (1999), 196-205.

Fredd, C. N., & Fogler, H. S. Influence of transport and reaction on wormhole formation in porous media. AIChE journal, 44(9), (1998), 1933-1949.

Fridleifsson, I. B., Bertani, R., Huenges, E., Lund, J. W., Ragnarsson, A., & Rybach, L. The possible role and contribution of geothermal energy to the mitigation of climate change, (2008), Paper presented at the IPCC scoping meeting on renewable energy sources, proceedings, Luebeck, Germany.

Garapati, N., Randolph, J. B., & Saar, M. O. Brine displacement by CO_2, energy extraction rates, and lifespan of a CO_2-limited CO_2-Plume Geothermal (CPG) system with a horizontal production well. Geothermics, 55(0), (2015), 182-194.

Garapati, N., Randolph, J. B., Valencia, J. L., & Saar, M. O. CO_2-Plume Geothermal (CPG) Heat Extraction in Multi-layered Geologic Reservoirs. Energy Procedia, 63, (2014), 7631-7643.

Gautier, J.-M., Oelkers, E. H., & Schott, J. Are quartz dissolution rates proportional to BET surface areas? Geochimica et Cosmochimica Acta, 65(7), (2001), 1059-1070.

Golubev, S. V., Pokrovsky, O. S., & Schott, J. Experimental determination of the effect of dissolved CO_2 on the dissolution kinetics of Mg and Ca silicates at 25 C. Chemical Geology, 217(3), (2005), 227-238.

Gong, Q., Deng, J., Han, M., Yang, L., & Wang, W. Dissolution of sandstone powders in deionised water over the range 50–350° C. Applied Geochemistry, 27(12), (2012), 2463-2475.

Gouze, P., & Luquot, L. X-ray microtomography characterization of porosity, permeability and reactive surface changes during dissolution. Journal of contaminant hydrology, 120, (2011), 45-55.

Hajash, A., Carpenter, T. D., & Dewers, T. A. Dissolution and time-dependent compaction of albite sand: Experiments at 100 °C and 160 °C in pH-buffered organic acids and distilled water. Tectonophysics, 295(1), (1998), 93-115.

Helgeson, H. C., Murphy, W. M., & Aagaard, P. Thermodynamic and kinetic constraints on reaction rates among minerals and aqueous solutions. II. Rate constants, effective surface area, and the hydrolysis of feldspar. Geochimica et Cosmochimica Acta, 48(12), (1984), 2405-2432.

Hirschberg, S., Wiemer, S., & Burgherr, P. Energy from the Earth: Deep Geothermal as a Resource for the Future? : vdf Hochschulverlag AG, (2014).

Hoefner, M., & Fogler, H. S. Pore evolution and channel formation during flow and reaction in porous media. AIChE journal, 34(1), (1988), 45-54.

IPCC. IPCC, 2005: IPCC special report on carbon dioxide capture and storage. Prepared by Working Group III of the Intergovernmental Panel on Climate Change. Cambridge, United Kingdom and New York, NY, USA, 442, (2005).

Kestin, J., Khalifa, H. E., & Correia, R. J. Tables of the dynamic and kinematic viscosity of aqueous NaCl solutions in the temperature range 20–150 C and the pressure range 0.1–35 MPa. Journal of physical and chemical reference data, 10(1), (1981), 71-88.

Kohl, T., Andenmatten, N., & Rybach, L. Geothermal resource mapping—example from northern Switzerland. Geothermics, 32(4), (2003), 721-732.

Kong, X.-Z., & Saar, M. O. Numerical study of the effects of permeability heterogeneity on density-driven convective mixing during CO_2 dissolution storage. International Journal of Greenhouse Gas Control, 19, (2013), 160-173.

Kong, X.-Z., & Saar, M. O. Determination of dissolution passages using X-ray computed tomography and volume registration techniques. (in prep.).

Landrot, G., Ajo-Franklin, J. B., Yang, L., Cabrini, S., & Steefel, C. I. Measurement of accessible reactive surface area in a sandstone, with application to CO_2 mineralization. Chemical Geology, 318, (2012), 113-125.

Li, L., Salehikhoo, F., Brantley, S. L., & Heidari, P. Spatial zonation limits magnesite dissolution in porous media. Geochimica et Cosmochimica Acta, 126, (2014), 555-573.

Luhmann, A. J., Kong, X.-Z., Tutolo, B. M., Ding, K., Saar, M. O., & Seyfried Jr, W. E. Permeability reduction produced by grain reorganization and accumulation of exsolved CO_2 during geologic carbon sequestration: A new CO_2 trapping mechanism. Environmental science & technology, 47(1), (2012), 242-251.

Luhmann, A. J., Kong, X.-Z., Tutolo, B. M., Garapati, N., Bagley, B. C., Saar, M. O., & Seyfried, W. E. Experimental dissolution of dolomite by CO_2-charged brine at 100 °C and 150 bar: Evolution of porosity, permeability, and reactive surface area. Chemical Geology, 380, (2014), 145-160.

Luquot, L., Andreani, M., Gouze, P., & Camps, P. CO_2 percolation experiment through chlorite/zeolite-rich sandstone (Pretty Hill Formation–Otway Basin–Australia). Chemical Geology, 294, (2012), 75-88.

Luquot, L., & Gouze, P. Experimental determination of porosity and permeability changes induced by injection of CO_2 into carbonate rocks. Chemical Geology, 265(1), (2009), 148-159.

Mao, S., & Duan, Z. The viscosity of aqueous alkali-chloride solutions up to 623 K, 1,000 bar, and

high ionic strength. International journal of thermophysics, 30(5), (2009), 1510-1523.

Nagy, K. L., Cygan, R. T., Hanchar, J. M., & Sturchio, N. C. Gibbsite growth kinetics on gibbsite, kaolinite, and muscovite substrates: atomic force microscopy evidence for epitaxy and an assessment of reactive surface area. Geochimica et Cosmochimica Acta, 63(16), (1999), 2337-2351.

Nami, P., Schellschmidt, R., Schindler, M., & Tischner, T. Chemical stimulation operations for reservoir development of the deep crystalline HDR/EGS system at Soultz-sous-Forêts (France), (2008), Paper presented at the Proceedings, 32nd Workshop on Geothermal Reservoir Engineering, Stanford University, Stanford, California, USA.

Peters, C. A. Accessibilities of reactive minerals in consolidated sedimentary rock: An imaging study of three sandstones. Chemical Geology, 265(1), (2009), 198-208.

Pokrovsky, O. S., Golubev, S. V., & Schott, J. Dissolution kinetics of calcite, dolomite and magnesite at 25 C and 0 to 50 atm pCO_2. Chemical Geology, 217(3), (2005), 239-255.

Pollack, H. N., Hurter, S. J., & Johnson, J. R. Heat flow from the Earth's interior: analysis of the global data set. Reviews of Geophysics, 31(3), (1993), 267-280.

Portier, S., André, L., & Vuataz, F.-D. Review on chemical stimulation techniques in oil industry and applications to geothermal systems. Engine, work package, 4, (2007), 32.

Portier, S., Vuataz, F.-D., Nami, P., Sanjuan, B., & Gérard, A. Chemical stimulation techniques for geothermal wells: experiments on the three-well EGS system at Soultz-sous-Forêts, France. Geothermics, 38(4), (2009), 349-359.

Pruess, K. Enhanced geothermal systems (EGS) using CO_2 as working fluid—a novel approach for generating renewable energy with simultaneous sequestration of carbon. Geothermics, 35(4), (2006), 351-367.

Randolph, J. B., & Saar, M. O. Coupling geothermal energy capture with carbon dioxide sequestration in naturally permeable, porous geologic formations-- a novel approach for expanding geothermal energy utilization (Vol. 73): Japan Association for Earthquake Engineering, (2011).

Rollin, K., & Institute of Geological Sciences, L. Investigation of the Geothermal Potential of the UK: A Review of Data Relating to Hot Dry Rock and Selection of Targets for Detailed Study: Institute of Geological Sciences, (1982).

Rose, P., Xu, T., Kovac, K., Mella, M., & Pruess, K. Chemical stimulation in near-wellbore geothermal formations: silica dissolution in the presence of calcite at high temperature and high pH, (2007), Paper presented at the Proceedings of Thirty-Second Workshop on Geothermal Reservoir Engineering, Stanford University, Stanford, California.

Rybach, L. The future of geothermal energy" and its challenges, (2010), Paper presented at the Proceedings World Geothermal Congress.

Saar, M. O. Review: Geothermal heat as a tracer of large-scale groundwater flow and as a means to determine permeability fields. Hydrogeology Journal, 19(1), (2011), 31-52.

Saar, M. O., Randolph, J. B., & Kuehn, T. H. Carbon Dioxide-based geothermal energy generation systems and methods related thereto. U.S. Patent No. 8,316,955 (issued 2012); Canada Patent No. 2.753.393 (issued 2013); Europe Patent No. 2406562 (issued 2014); Australia Patent No. 2010223059 (issued 2015). the Regents of the University of Minnesota, (2012-2015).

Schill, E., Cuenot, N., Genter, A., & Kohl, T. Review of the Hydraulic Development in the Multi-Reservoir/Multi-Well EGS Project of Soultz-sous-Forêts, (2015), Paper presented at the Proceedings World Geothermal Congress.

Taron, J., & Elsworth, D. Thermal–hydrologic–mechanical–chemical processes in the evolution of engineered geothermal reservoirs. International Journal of Rock Mechanics and Mining Sciences, 46(5), (2009), 855-864.

Tester, J. W., Anderson, B., Batchelor, A., Blackwell, D., DiPippo, R., Drake, E., . . . Nichols, K. The future of geothermal energy: Impact of enhanced geothermal systems (EGS) on the United States in the 21st century. Massachusetts Institute of Technology, 209, (2006).

The KamLAND collaboration. Partial radiogenic heat model for Earth revealed by geoneutrino measurements. Nature Geoscience, 4(9), (2011), 647-651.

Tutolo, B. M., Luhmann, A. J., Kong, X.-Z., Saar, M. O., & Seyfried Jr, W. E. Experimental observation of permeability changes in dolomite at CO2 sequestration conditions. Environmental science & technology, 48(4), (2014), 2445-2452.

Tutolo, B. M., Luhmann, A. J., Kong, X.-Z., Saar, M. O., & Seyfried, W. E. CO_2 sequestration in feldspar-rich sandstone: Coupled evolution of fluid chemistry, mineral reaction rates, and hydrogeochemical properties. Geochimica et Cosmochimica Acta, 160, (2015), 132-154.

Washton, N. M., Brantley, S. L., & Mueller, K. T. Probing the molecular-level control of aluminosilicate dissolution: A sensitive solid-state NMR proxy for reactive surface area. Geochimica et Cosmochimica Acta, 72(24), (2008), 5949-5961.

White, A. F., Blum, A. E., Bullen, T. D., Vivit, D. V., Schulz, M., & Fitzpatrick, J. The effect of temperature on experimental and natural chemical weathering rates of granitoid rocks. Geochimica et Cosmochimica Acta, 63(19), (1999), 3277-3291.

White, A. F., & Brantley, S. L. The effect of time on the weathering of silicate minerals: why do weathering rates differ in the laboratory and field? Chemical Geology, 202(3), (2003), 479-506.

White, A. F., & Peterson, M. L. Role of reactive-surface-area characterization in geochemical kinetic models, (1990), Paper presented at the ACS symposium series.

Woodside, W., & Messmer, J. H. Thermal conductivity of porous media. I. Unconsolidated sands. Journal of applied physics, 32(9), (1961a), 1688-1699.

Woodside, W., & Messmer, J. H. Thermal conductivity of porous media. II. Consolidated rocks. Journal of applied physics, 32(9), (1961b), 1699-1706.

Xu, T. Numerical simulation to study the feasibility of using CO_2 as a stimulation agent for enhanced geothermal systems. Lawrence Berkeley National Laboratory, (2010).

Acknowledgements

We thank Dr. Andrew Luhmann from New Mexico Institute of Mining and Technology, USA and Dr. Benjamin Tutolo from University of Oxford, UK for the helpful discussions. We also thank research support from the DESTRESS H2020 and ETH Research Grant ETH-12 15-2, as well as the Werner Siemens Stiftung/Endowment for its support of the Geothermal Energy and Geofluids Group.